Journal of Alloys and Compounds 890 (2021) 161919

Contents lists available at ScienceDirect

Journal of Alloys and Compounds

journal homepage: www.elsevier.com/locate/jalcom

Ultra-fast construction of $CuBi_2O_4$ films supported Bi_2O_3 with dominant (0 2 0) facets for efficient CO_2 photoreduction in water vapor

Weina Shi[a,c], Ji-Chao Wang[b,*], Xiaowei Guo[a,c], Hong-Ling Tian[b], Wanqing Zhang[b], Huiling Gao[b], Huijuan Han[b], Renlong Li[b], Yuxia Hou[b,*]

[a] School of Chemistry and Materials Engineering, Xinxiang University, Xinxiang 453000, China
[b] College of Chemistry and Chemical Engineering, Henan Institute of Science and Technology, Xinxiang 453000, China
[c] Henan Photoelectrocatalytic Material and Micro-Nano Application Technology Academician Workstation, Xinxiang University, Xinxiang 450003, China

ARTICLE INFO

Article history:
Received 30 May 2021
Received in revised form 6 August 2021
Accepted 6 September 2021
Available online 11 September 2021

Keywords:
Photocatalysis
CO_2 reduction
$CuBi_2O_4/Bi_2O_3$
Exposed facets
S-scheme

ABSTRACT

$CuBi_2O_4/Bi_2O_3$ thin film was synthesized on the commercial glass by a spray pyrolysis-calcination method. The monoclinic phase Bi_2O_3 with dominant (0 2 0) facets was grown on the surface of tetragonal phase $CuBi_2O_4$ by the temperature control of spraying process. Photocatalytic activities of the synthesized materials for CO_2 reduction were measured in the presence of water vapor under visible light irradiation (λ > 400 nm). The CO, CH_4 and O_2 yields of the optimal composite film reached 247.62, 119.27 and 418.00 μmol/m^2 after 12 h of irradiation. The composite film resisted physical damage and showed good photocatalytic activity in the cycling tests. Moreover, it was found that the types of main products changed with the light intensity and their yields varied with the light wavelength. The exposed (0 2 0) facets efficiently improved the adsorbed ability for H_2O molecules. Meanwhile, the hydrophobicity of the film surface ensured that the adsorbed sites of CO_2 were unoccupied by abundant H_2O molecules. The S-scheme charge transfer mechanism was further confirmed by the interlaced band alignment of the $CuBi_2O_4/Bi_2O_3$ heterostructure and the controlled experiment with different light conditions. The results gained in this report may open up an avenue to design advanced S-scheme heterostructures with suitable transitional-metal oxides for photoreduction CO_2 to solar fuels.

1. Introduction

Artificial photosynthesis of converting CO_2 and H_2O into hydrocarbon fuel is an eminently promising strategy to cope with fleetly increased energy demand and greenhouse gas (mainly CO_2) emissions [1,2]. Yet, the CO_2 hydrogenation process needs a bond dissociation energy of more than 120 kcal/mol, resulting in the high activation energy in conversion process [3–5]. The CO_2 photoreduction using semiconductor catalysts is a renewable and promising technique to produce valuable carbon derivatives [6,7]. However, in the conventional photocatalytic system (liquid-solid two-phases system), only CO_2 dissolved in the water was utilized because the hydrogen source for the CO_2 conversion should be ideally supplied by water molecules [8]. Due to the poor solubility and slow diffusion rate of CO_2 in water, the competing hydrogen evolution reaction of water reduction was dominant. Hence, the photocatalytic activity for CO_2 reduction over semiconductor catalyst can be promoted by controlling photocatalytic structures for direct delivery of gas phase CO_2 and H_2O to the photocatalytic reaction interface.

Since the adsorbed CO_2 molecules on the catalyst surface can be rapidly depleted under strong reaction driving force, the supply of CO_2 molecules is usually critical for efficient CO_2 photoreduction [9,10]. Meanwhile, the H_2O adsorption and activation on the catalyst surface can not be omitted in CO_2 conversion process, because of the high overpotential for H_2O oxidation reaction [10]. Although porous nanomaterials usually possess large surface-to-volume ratios, the surface adsorption sites for H_2O molecules are still insufficient, leading to low concentration and slow diffusivity of H_2O molecules at the catalyst surface [11]. Hence, enhancing adsorption capacity of reactant molecules on catalyst is conducive to increase the concentration and transfer rate of CO_2 reduction and H_2O oxidation at the catalyst surface, further boosting CO_2 reduction and suppressing the hydrogen evolution reaction. The influence of exposed crystal facets of semiconductor catalyst is never ignored [12,13]. Chen et al. synthesized shell like TiO_2 with exposed (001) facets for enhanced

* Corresponding authors.
E-mail addresses: wangjichao@hist.edu.cn (J.-C. Wang), yxhou@163.com (Y. Hou).

https://doi.org/10.1016/j.jallcom.2021.161919
0925-8388/

photocatalytic CO_2 reduction in gas-solid system, and proved that {001} and {101} facets acted as reduction sites and oxidation sites, respectively [14]. Moreover, the rapid recombination of photo-induced electron-hole pairs and wide band gap for a single component semiconductor limit the application of CO_2 photoreduction [15–17]. The heterojunction construction not only promotes the separation of photo-generated carriers, but also adjusts distribution of oxidation and reduction sites on the photocatalyst surface [18,19]. In particular, Step scheme (S-scheme) heterojunction photocatalytic system is highly recommended due to the promoted separation of photo-induced electrons and holes without sacrificing their redox abilities [20–24]. Therefore, the controlled formation of S-scheme composite with specific exposed facets could realize the adsorption ability and selectivity for H_2O or CO_2 molecules of the reaction site on photocatalyst surface. Additionally, it is always difficult to process the complete separation of powdered catalyst from catalytic system, causing second pollution for heterogeneous photocatalytic system [25,26]. Hence, thin film photocatalyst has gradually been paid great attention due to its larger surface area and easier recycling [25,27,28].

$CuBi_2O_4$ has recently received scientific interest as a promising candidate due to its suitable bandgap of 1.5–1.8 eV and negative conduction band location [29–31], enabling thermodynamically feasible for photocatalytic CO_2 reduction. Nonetheless, photocatalytic CO_2 reduction with H_2O was not achievable for mono-component $CuBi_2O_4$ due to its higher VB potential than the oxidation potential of O_2/H_2O. On the basis, heterojunction construction has been proposed to mitigate the limitation of single $CuBi_2O_4$ [32–34]. Bi_2O_3 has been studied as a promising photocatalyst due to its strong oxidizability and appropriate band gap for visible light absorption [32,35,36], enabling hybridization with $CuBi_2O_4$ to construct heterojunction composites with increased light harvesting property, prolonged lifetime of carriers and enhanced catalytic performance [37,38]. Particularly, the $CuBi_2O_4/Bi_2O_3$ composite was reported to exhibit superior performance for photocatalytic degradation [39]. Nevertheless, the research of $CuBi_2O_4/Bi_2O_3$ film is scarcely focused on photocatalytic CO_2 reduction up till now.

In this study, we synthesized a series of $CuBi_2O_4/Bi_2O_3$ composite films on the glass substrates by the spray pyrolysis method. The influence of the spraying temperature on the growth of Bi_2O_3 nanoparticle in composite was studied. Photocatalytic activities of CO_2 reduction over the $CuBi_2O_4/Bi_2O_3$ films were investigated in the presence of water vapor. Compared to the bare materials, the as-prepared $CuBi_2O_4/Bi_2O_3$ composites were found to exhibit highly improved photocatalytic performance, and the selectivity was able to be tuned by modulating the light intensity. The enhanced catalytic activity was attributed to efficient charge separation originated from the staggered band structure, and a S-scheme charge transfer mechanism was further proposed and confirmed.

2. 2. Experimental section

2.1. Synthesis of $CuBi_2O_4$, Bi_2O_3 and $CuBi_2O_4/Bi_2O_3$ films

The commercial glass substrates were cleaned by ethanol and deionized water before use. $CuBi_2O_4$, Bi_2O_3 and $CuBi_2O_4/Bi_2O_3$ films were deposited on the substrates by the spray pyrolysis method. In the typical synthesis of $CuBi_2O_4$ films supported Bi_2O_3 with dominant (0 2 0) facets, two precursor solutions were prepared by dissolving 0.4484 g $Bi(NO_3)_3{\cdot}5H_2O$ in 2 mL acetic acid and 0.0960 g $Cu(NO_3)_2{\cdot}3H_2O$ in 38 mL ethanol, respectively. The solutions were then mixed and sprayed onto the glass substrates at 260 °C, and the final sample was annealed at 500 °C for 2 h. The obtained composite film was abbreviated as CBO/BO-020.

For comparison, bare $CuBi_2O_4$ and Bi_2O_3 films were obtained by the similar spray pyrolysis procedure using the corresponding precursors. Additionally, Bi_2O_3 nanoparticles were obtained from the bare Bi_2O_3 film by ultrasound treatment. The physically mixed CBO/BO-M film was prepared by spraying the alcoholic suspension, which contained the Bi_2O_3 and $CuBi_2O_4$ particles though scraped off the glass substrates. In addition, CBO/BO-020-P film was obtained by physical damage treatment of the CBO/BO-020 sample, and the experiment details were illustrated in Fig. S1.

The $CuBi_2O_4$ film supported Bi_2O_3 without dominant (0 2 0) facets, abbreviated as CBO/BO, was obtained by the spray pyrolysis method similar to CBO/BO-020, except that the spray-drying temperature was 150 °C. The contents of metal ions for all of the obtained samples were detected by ICP-AES measurements, and the real Bi/Cu ratios (Table S1) in the composites were basically consistent with initial inventory ratio.

2.2. Characterization

The crystal structures and phases of the obtained samples were studied by the D8 Advance powder X-ray diffractometer (Bruker Technology Co., Ltd.) with Cu Kα radiation (λ = 1.5418 Å). The chemical components and valence states were analyzed using the X-ray photoelectron spectrometer (XPS, PHI5000 VersaProbe, ULVAC-PHI Inc., Japan). The material morphology was measured by field emission scanning electron microscope (FE-SEM, NANO SEM430, FEI, USA). The images of transmission electron microscopy (TEM) were recorded by the JEM-2100 electron microscope (JEOL Ltd., Japan). The UV–vis diffuse reflectance spectra (DRS) were obtained using the UV–vis-NIR spectrometer (Cary 5000, Agilent Technology Co., Ltd., USA).

2.3. Photocatalytic performance tests

The photocatalytic performance for CO_2 reduction was investigated in the gas-solid phase catalytic system with 0.16 MPa pressure. The reactant gas was composed of high purity CO_2 gas (99.999%) and water vapor. A 300 W xenon arc lamp (PLS-SXE300, Beijing China Eduction Au-Light Co., Ltd., China) with a UV cutoff filter was adopted as the light source in the photocatalytic reactions. The gaseous and liquid products were detected by gas chromatograph (GC-7890II, Beijing China Eduction Au-Light Co., Ltd., China) and GC-MS (7890A-5975C, Agilent Technology Co., Ltd., USA), respectively. The isotopes tracer experiments were performed in a sealed reactor. The $^{13}CO_2$ or $H_2{}^{18}O$ reactants were added into the sealed reactor. After UV light irradiation of 18 h, the gas mixture in container was measured by GC-MS (7890A-5975C and MAT 271). The experiment process was detailed in Supporting Information S1. Photoelectrochemical test and electrochemical impedance spectroscopy (EIS) measurement were performed in a conventional three-electrode system using the electrochemical workstation (CHI 660E, Shanghai Chenhua Co., Ltd., China). The H_2O_2 capture tests for photocatalyst were also detailed in Supporting Information S2.

3. Results and discussion

3.1. Structure, morphology and composition

Fig. 1 showed the XRD patterns of the obtained samples. The distinct peaks of $CuBi_2O_4$ sample at 20.8°, 27.9°, 30.7°, 33.2°, 37.4°, 46.6° and 52.9° were corresponding to (2 0 0), (2 1 1), (0 0 2), (3 1 0), (2 0 2), (4 1 1) and (2 1 3) facets of tetragonal phase $CuBi_2O_4$ (JCPDs No: 48-1886), respectively. Besides, the diffraction peaks of bare Bi_2O_3 sample indicated the formation of monoclinic phase (JCPDs No: 14-0699). In addition to the peaks originated from $CuBi_2O_4$ in the composites, the other characteristic peaks at 25.8°, 26.9°, 27.4°, 33.1° and 33.2° were indexed to (0 2 0), (1 1 1), (−1 2 0), (1 2 1) and (2 0 0) crystal facets of Bi_2O_3. The peak intensity at 21.7° in the CBO/

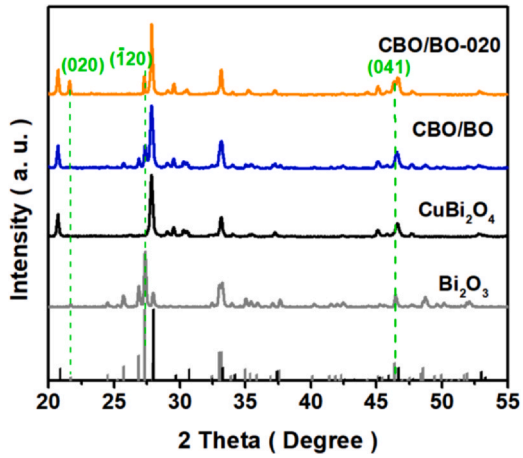

Fig. 1. XRD patterns of the obtained bare and composite samples.

BO-020 sample was obviously stronger than those of CBO/BO and bare Bi_2O_3 samples. By measuring the respective peak areas of the (0 2 0), (−1 2 0), (1 2 1) and (2 0 0) facets, the fraction of (0 2 0) facets from XRD patterns were estimated by the following equation (Eq. (1)):[12].

$$w_{(0\ 2\ 0)} = [\Sigma A_{(0\ 2\ 0)}/\Sigma A_{(0\ 2\ 0)} + \Sigma A_{(-1\ \ 2\ 0)} + \Sigma A_{(1\ 2\ 0)} + \Sigma A_{(2\ 0\ 0)}] \quad (1)$$

The calculated percentage of (0 2 0) facets for CBO/BO and CBO/BO-020 were about 2.2% and 36.8%, respectively. It indicated that the (0 2 0) crystal facet of Bi_2O_3 grew well in the presence of $CuBi_2O_4$. For further exploring the effect of the growth of (0 2 0) facets, a series of composite samples with different spray-drying temperatures were obtained by the similar method. According to the XRD results (Fig. S2), with increasing the spray-drying temperature, the peak intensity of (0 2 0) facets in the composites gradually increased. Therefore, the spray-drying temperature influenced facet growth of the precursor, leading to the development of (0 2 0) facet of Bi_2O_3 in the composites.

The composition and valance states of the obtained samples were studied by XPS measurements. The high-resolution spectrum of Cu 2p was shown in Fig. 2a, and the two distinct peaks centered at 934.1 eV and 954.1 eV were corresponding to Cu $2p_{3/2}$ and Cu $2p_{1/2}$ of Cu(II), respectively [38,40]. Besides, the satellite peaks were distinctly observed due to a d^9 configuration in the ground state of Cu(II)-based oxides [41]. The deconvolution result of Bi 4f core level spectrum was shown in Fig. 2b. Two obvious peaks at binding energies of 159.4 eV and 163.6 eV were assigned to Bi $4f_{7/2}$ and Bi $4f_{5/2}$, which were in consistent with those of Bi (III)-based oxides [33,41,42]. Additionally, the deconvolution peaks of O 1s spectrum (Fig. 2c) were resolved into two components originated from lattice oxygen and surface oxygen defects [29,38,43]. It was noteworthy that the peaks of bare Bi_2O_3 and $CuBi_2O_4$ samples were slightly shifted compared with those of the CBO/BO-020 composite, which indicated the successful formation of CBO/BO-020 heterojunction [38].

The cross sectional images of the $CuBi_2O_4$, Bi_2O_3 and CBO/BO-020 samples were shown in Fig. 3a–c. The height of the thin film was about 1.1 μm, and the Cu, Bi, and O elements were homogenously distributed as indicated in the EDS mapping images. Moreover, the

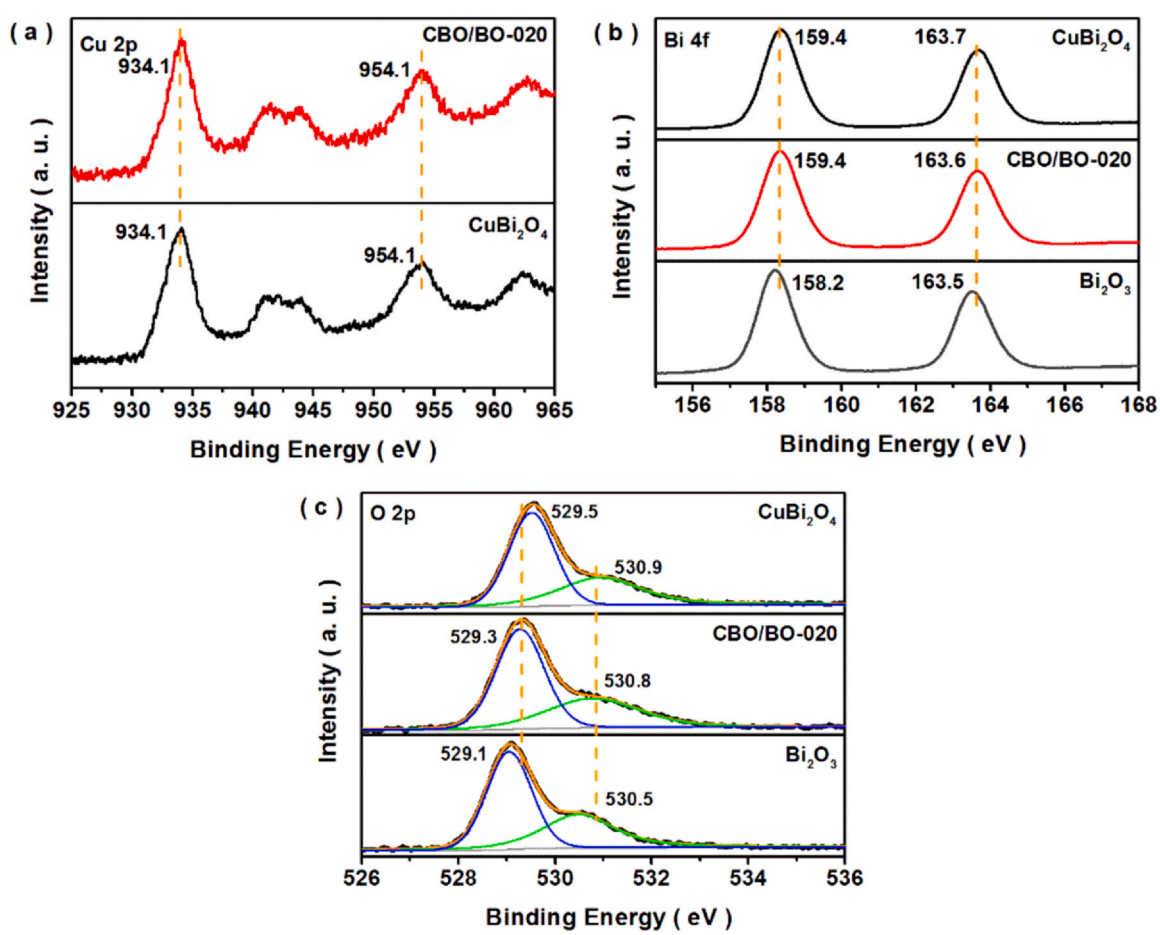

Fig. 2. XPS spectra (a. Cu 2p, b. Bi 3p and c. O 2p) of the $CuBi_2O_4$, Bi_2O_3 and CBO/BO-020 samples.

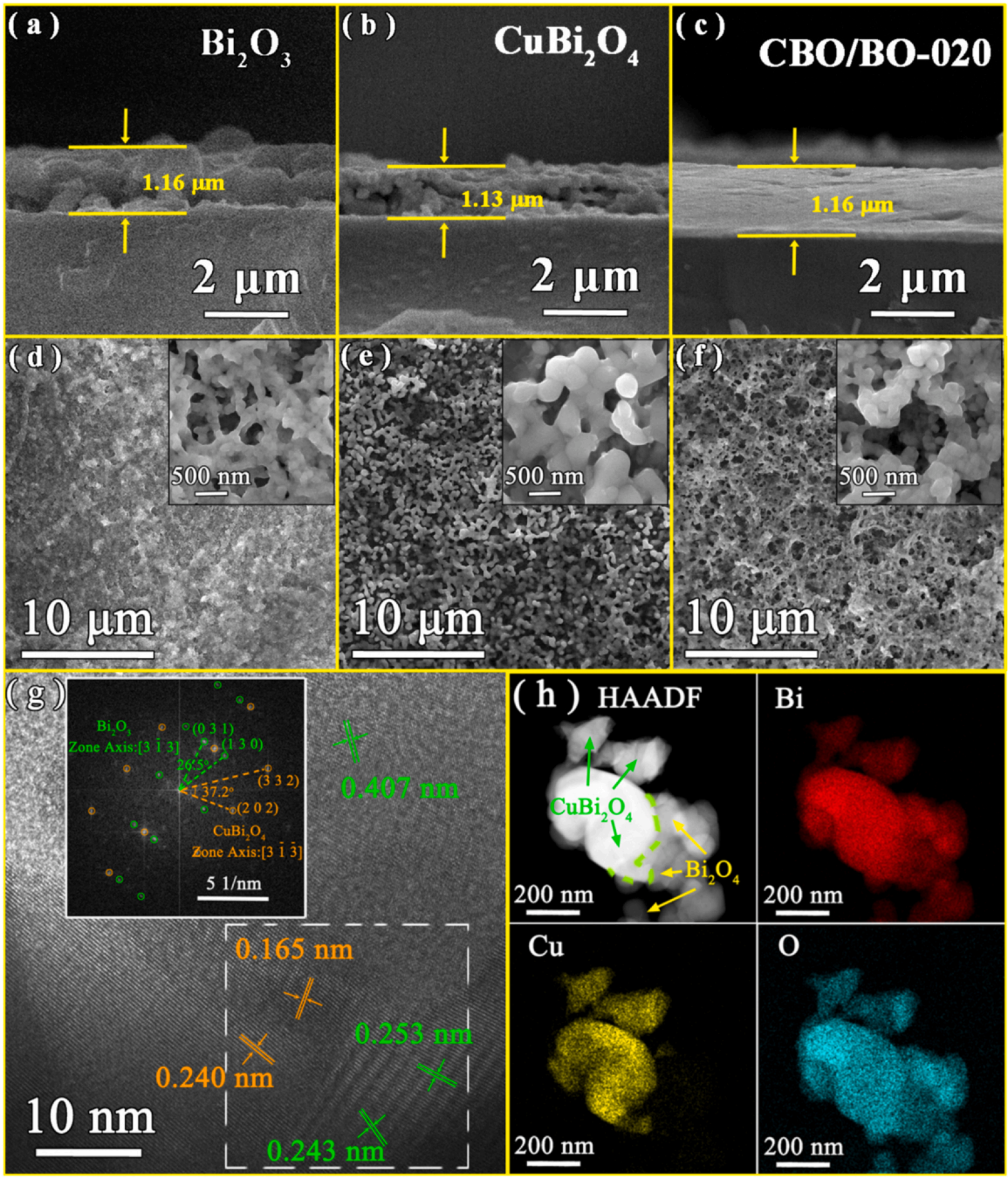

Fig. 3. SEM images of (a, d) Bi_2O_3, (b, e) $CuBi_2O_4$ and (c, f) CBO/BO-020 samples and TEM image (g, h) of CBO/BO-020 sample.

morphology of pore structure was observed for all the samples, and the surface area of CBO/BO-020 was slightly higher than those of Bi_2O_3 and $CuBi_2O_4$ (Table S2). The morphology and composition of the obtained samples were shown in Fig. 3d–h. All the films were composed of uniformly dispersed nanoparticles, and the particle size of Bi_2O_3 (Fig. 3d) was smaller compared with those of $CuBi_2O_4$ (Fig. 3e) and CBO/BO-020 (Fig. 3f). The TEM image of CBO/BO-020 in Fig. 3g indicated that the interplanar spacings of 0.165 and 0.240 nm corresponded to (3 3 2) and (2 0 2) facets of tetragonal phase $CuBi_2O_4$, and the interplanar spacings of 0.253, 0.243 and 0.407 nm were assigned to (0 3 1), (1 3 0) and (0 2 0) facets of monoclinic phase Bi_2O_3. Fast-Fourier Transform (FFT) diffraction pattern (inset of Fig. 3g) of the selected dotted bordered rectangle region confirmed the existence of tetragonal $CuBi_2O_4$ and monoclinic Bi_2O_3, which were consistent with XRD results. Hence, the TEM observations and FFT pattern of the CBO/BO-020 composite revealed that both $CuBi_2O_4$ and Bi_2O_3 were present and fused at the interfaces. The HAADF-STEM image and corresponding EDX mapping of CBO/BO-020 in Fig. 3h presented uniform distribution of Bi and O elements in the composite. Cu element only appeared on the surface of larger particles, and it was concluded that Bi_2O_3 was successfully deposited on the $CuBi_2O_4$ surface. Combined with the SEM and XRD results, it

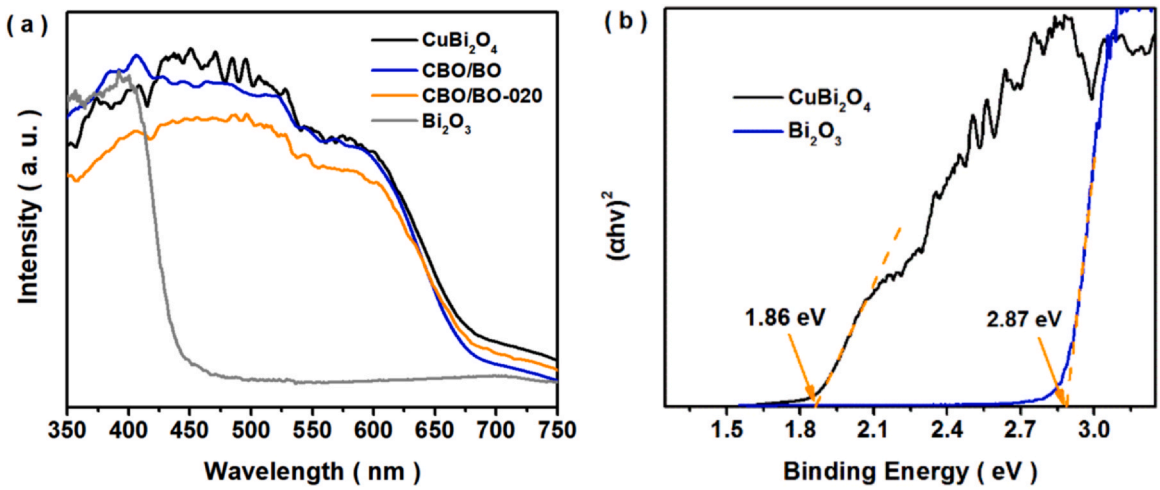

Fig. 4. DRS spectra (a) and plots of $(\alpha h\nu)^2$ versus $h\nu$ (b) of the obtained samples.

was concluded that smaller Bi_2O_3 particles were successfully deposited on the $CuBi_2O_4$ surface. The rough surface of the composite film was formed by two kinds of nanoparticles, which further leaded to specific hydrophilia ability of the composite photocatalyst.

Fig. 4a showed the UV-Vis light absorption spectra of the obtained samples. All the obtained composite samples and $CuBi_2O_4$ sample exhibited broad photoresponse range of up to 650 nm. The direct band gaps (E_g) of $CuBi_2O_4$ and Bi_2O_3 samples estimated by the Kubelka-Munk function (Fig. 4b) were 1.86 and 2.87 eV, respectively, agreeing well with previously reported values [44,45].

3.2. Photocatalytic performance

The photocatalytic performance for CO_2 reduction with water vapor was studied under visible light illumination. No products were detected for CO_2 reduction without photocatalyst or illumination in the catalytic system. As shown in Fig. 5a, no product was detected for bare Bi_2O_3, and a small quantity of CO was produced over $CuBi_2O_4$ sample. Moreover, all the composites exhibited higher photocatalytic activities of CO_2 reduction than those of bare Bi_2O_3 and $CuBi_2O_4$. Particularly, the CBO/BO-020 sample with high intensity of (0 2 0) facets for Bi_2O_3 exhibited inferior photocatalytic activity, and the CO, CH_4 and O_2 yields of CBO/BO-020 reached 127.13, 70.10 and 231.95 μmol/m^2, respectively. The yields of CBO/BO-020 for CO_2 reduction were higher than those in the previous studies of Bi_2O_3 based materials (Table S3). To exclude the possibility of the produced fuels generated from other synthesis residues, ^{13}C and ^{18}O labeled isotopic tests were implemented by substituting $^{12}CO_2/H_2{}^{16}O$ with $^{13}CO_2/H_2{}^{18}O$. The results of GC-MS tests for the products were presented in Fig. 5b. Besides, the CO and CH_4 yields of CBO/BO-020-M obviously decreased compared with those of CBO/BO-020, indicating that the loosely contacted interfaces were insufficient for photocatalytic CO_2 reduction. It indicated that the formation of heterojunction promoted the photocatalytic activity for CO_2 reduction [18]. Additionally, the CO, CH_4 and O_2 yields of CO_2 reduction over CBO/BO-020-P sample still reached 132.21, 66.05 and 201.11 μmol/m^2, respectively, indicating that the CBO/BO-020 composite film on the glass resisted physical damage, which was valuable in photocatalytic application. Hence, the CBO/BO-020 composite photocatalyst exhibited satisfactory performance for photocatalytic CO_2 reduction with water vapor. The influences of light wavelength and intensity on photocatalytic activity and kinds

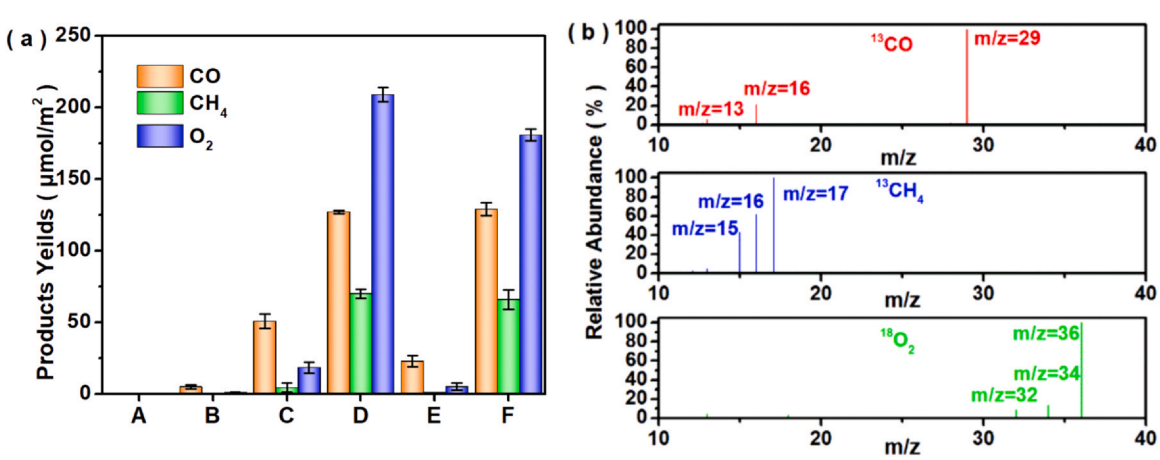

Fig. 5. Product yields over the composites for photocatalytic CO_2 reduction with water vapor under visible-light irradiation (a: A. Bi_2O_3, B. $CuBi_2O_4$, C. CBO/BO, D. CBO/BO-020, E. CBO/BO-020-M and F. CBO/BO-020-P) and Mass spectra of ^{13}CO, $^{13}CH_4$ and $^{18}O_2$ products over the CBO/BO-020 photocatalyst for CO_2 photoreduction (b).

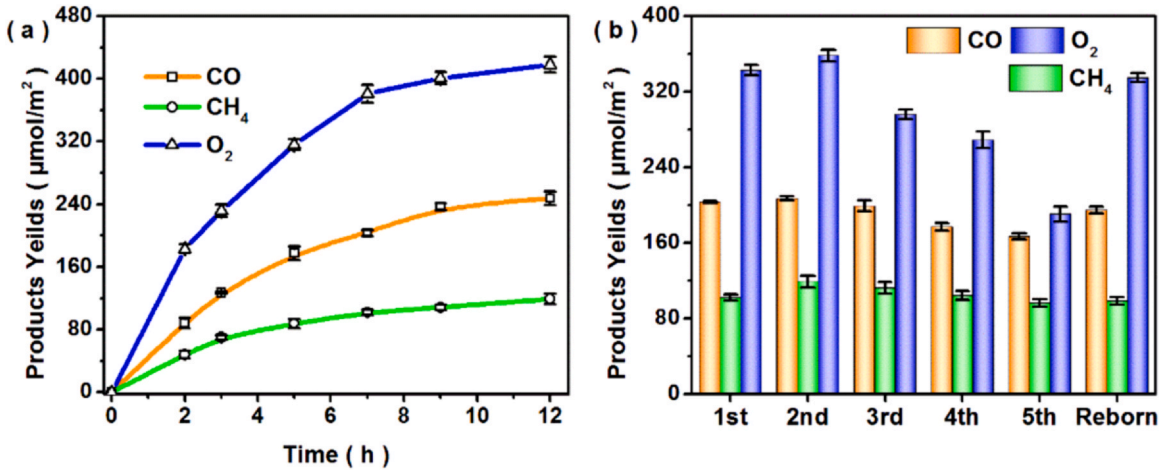

Fig. 6. Total yields (a) and durability test (b) of CBO/BO-020 for photocatalytic CO_2 reduction with water vapor (each cycle illuminated for 7 h).

of products for CO_2 reduction were also investigated. In Table S4, CO and CH_4 yields over the CBO/BO-020 catalyst changed slightly when the light wavelength range was widened. However, with increase of light intensity, the product yields of CO_2 reduction obviously increased and the molar ratio of CH_4/CO was improved. CO was the main product at 320 mW/cm^2, and the total yield increased significantly in comparison with those at 80, 230 and 230 mW/cm^2. Besides, the minor product of CH_4 was also observed with the light intensity of above 230 mW/cm^2. The results suggested that the photocatalytic properties of the photocatalyst were greatly related to the intensity of irradiation light, which was consistent with the results in previous study [46]. Based on the above results, the product yields were mainly dependent on light intensity for photocatalytic CO_2 reduction.

Fig. 6a showed the product yields for CO_2 reduction over CBO/BO-020 sample with visible-light illumination time prolonging. The CO, CH_4 and O_2 yields of CBO/BO-020 continually increased, and the yield rates reached 20.64, 9.94 and 34.83 μmol/m^2/h under light irradiation for 12 h. The photocatalytic stability of the typical CBO/BO-020 catalyst was measured by a five-time durability test, and the results were shown in Fig. 6b. The yields of CO and CH_4 slightly decreased and reached 167.03 and 96.44 μmol/m^2 after five cycles. XRD and XPS measurements were further conducted to study the stability of photocatalyst after the durability test. As shown in Figs. S3 and S4, there were no obvious differences in the crystal structure and chemical state between the fresh and used photocatalysts. However, the O_2 yield obviously decreased. According to the results of the H_2O_2 capture tests (Fig. S5), the H_2O_2 molecules were formed and remained on the surface after illumination. It implied that the oxidation site on the photocatalyst may be occupied by the intermediate products and then resulted in its deactivation. The used CBO/BO-020 catalyst was regenerated by sodium sulfite treatment. It was notable that the products yields of regenerated catalyst obviously increased. Hence, the decrease photocatalytic activity was caused by the toxicity of H_2O_2 molecules for the active sites on the composite surface.

3.3. Photocatalytic mechanism

As shown in Fig. 7, the transient photocurrent responses of Bi_2O_3, $CuBi_2O_4$, CBO/BO and CBO/BO-020 were measured over several

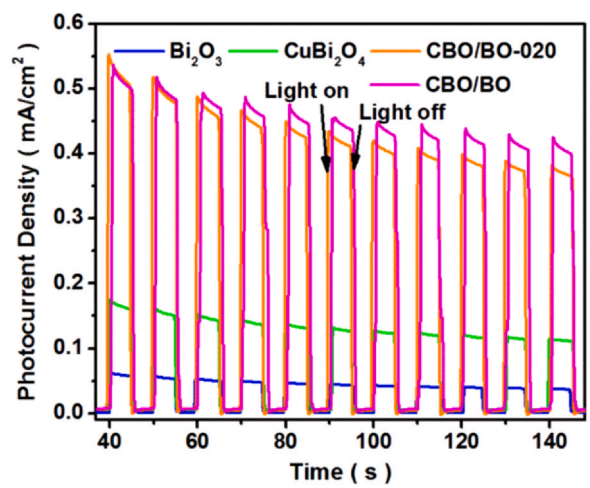

Fig. 7. Transient photocurrent responses of Bi_2O_3, $CuBi_2O_4$, CBO/BO and CBO/BO-020 catalysts.

on-off irradiation cycles. The transient photocurrent densities of composites were about 3 and 9 times higher than those of $CuBi_2O_4$ and Bi_2O_3, respectively. Hence, the formation of heterojunction played a key role in promoting the separation of photo-generated electrons and holes.

For exploring the band structure of $CuBi_2O_4$ and Bi_2O_3, the VB-XPS measurement was investigated and the result was shown in Fig. 8. The VB values of $CuBi_2O_4$ and Bi_2O_3 were calculated by the linear intersection method and reached 1.05 and 3.02 eV, respectively [46]. According to the E_g values of the obtained samples (Fig. 4b), the CB positions of $CuBi_2O_4$ and Bi_2O_3 were determined to be −0.81 and 0.15 eV, respectively. The staggered Type II band alignment was thus formed in the $CuBi_2O_4/Bi_2O_3$ composite.

Based on the band energy alignment of the $CuBi_2O_4$ and Bi_2O_3 composite (Fig. 9), the p-n heterojunction was established by tight contact between the Bi_2O_3 and $CuBi_2O_4$ components, and an inner electrical field was formed at the interface, facilitating the transfer of photo-induced carriers. In the case of the common double-charge transfer mode in the heterojunction (Fig. 9a), the

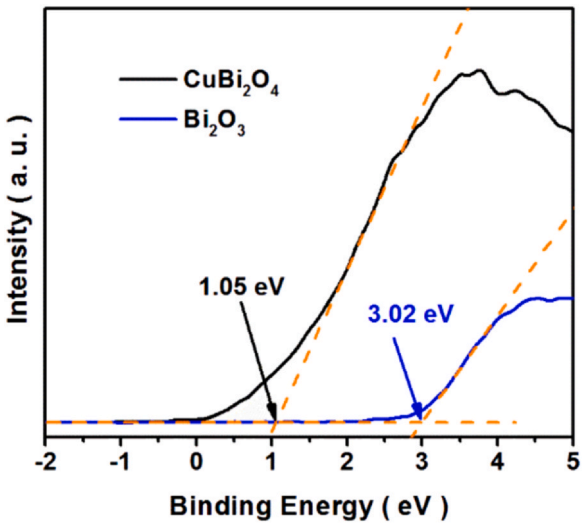

Fig. 8. VB-XPS spectra of the obtained $CuBi_2O_4$ and Bi_2O_3 samples.

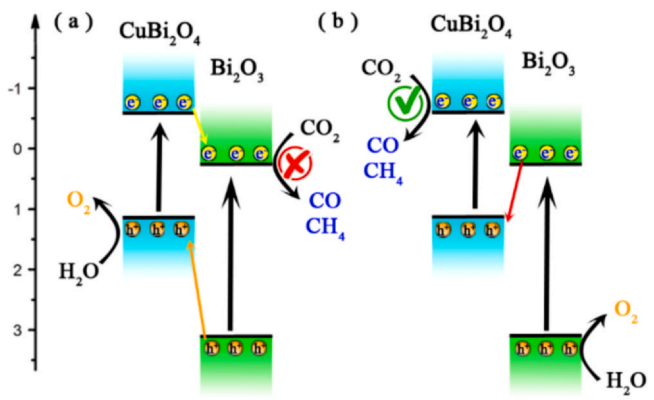

Fig. 9. Schematic diagram for the common transfer mode (a) and S-scheme transfer mode (b) of photo-induced carrier in the $CuBi_2O_4/Bi_2O_3$ composites.

accumulated electrons in the CB of Bi_2O_3 with insufficient reduction ability would not drive CO_2 reduction due to the more positive redox potentials of CO_2/CO (−0.53 V) and CO_2/CH_4 (−0.24 V) [47], which was inconsistent with the experimental results. According to the above photocatalytic results, CO was produced over CBO/BO-020 under irradiation of 400–800 nm with light intensity of 80 mW/cm^2 (Table S4). The control experiment was carried out under the similar condition except for the light source with wavelength range of 635–665 nm. Since the visible light solely excited $CuBi_2O_4$ in the composite, and the photogenerated electrons would transfer from the CB of $CuBi_2O_4$ to that of Bi_2O_3 for CO_2 reduction. Yet, few CO product was detected. Based on the promoted photocatalytic performance, a S-scheme mechanism was proposed and illustrated in Fig. 9b. Photo-induced electrons in the CB of Bi_2O_3 recombined with photo-induced holes in the VB of $CuBi_2O_4$ (Fig. 9b), and the composite retained strong reduction ability of electrons in the CB of $CuBi_2O_4$, and CO_2 can be reduced to CO and CH_4 readily. Meanwhile, the photoinduced holes in the VB of Bi_2O_3 easily realized H_2O oxidation [48]. Consequently, the S-scheme heterojunction was formed in the $CuBi_2O_4/Bi_2O_3$ composite photocatalyst.

Although the photocurrent density of CBO/BO was similar with that of CBO/BO-020, the CBO/BO-020 sample exhibited higher photocatalytic performance. The exposed (0 2 0) facets of Bi_2O_3 may play a key role for photocatalytic process of CO_2 reduction with water vapor. As shown in Fig. 10a, the H_2O adsorption ability of CBO/BO-020 was distinctly stronger than that of CBO/BO, because of the exposed (0 2 0) facets of Bi_2O_3 composition. Combined with the analysis of the electron transfer in heterojunction, it was thus speculated that H_2O oxidation reaction occurred on the Bi_2O_3 surface in the composite. Yet, as shown in Fig. 10b and c, the wetting angles of CBO/BO-020 and CBO/BO reached about 133° and 118°, respectively, due to the porous structure on the films surface, and all composites exhibited stronger hydrophobicity. Although abundant H_2O molecules were adsorbed on the surface of the CBO/BO-020 sample, the adsorbed sites of CO_2 on the surface were unoccupied by the stronger hydrophobicity [8]. Hence, the exposed (0 2 0) facets of Bi_2O_3 in the composites improved the adsorbed property for H_2O molecules on the photocatalyst surface, leading to enhanced CO_2 photoreduction performance.

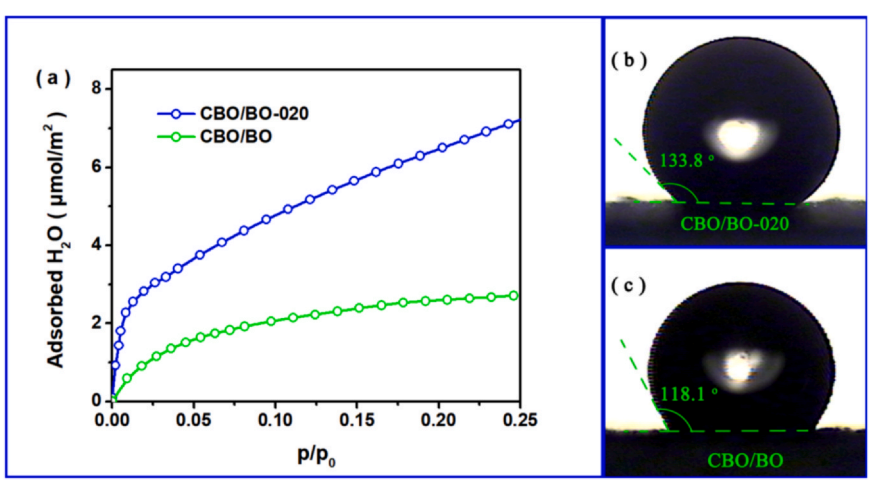

Fig. 10. H_2O adsorption curves (a) and wetting angle images (b and c) of the CBO/BO-020 and CBO/BO samples.

4. Conclusion

In summary, a series of composite films containing of monoclinic Bi_2O_3 with dominant (0 2 0) facets and tetragonal $CuBi_2O_4$ were synthesized on the surface of commercial glasses by a spray pyrolysis-calcination method. The temperature control of spraying process influenced the growth of Bi_2O_3 particle on the $CuBi_2O_4$ surface. The CO, CH_4 and O_2 yields of the optimal $CuBi_2O_4/Bi_2O_3$ composite reached 247.62, 119.27 and 418.00 μmol/m^2 after 12 h of visible-light irradiation for CO_2 reduction, and the photocatalyst showed good photocatalytic activity after 5 cycles. The type of main products changed with the light intensity. The exposed (0 2 0) facet of Bi_2O_3 improved the adsorbed ability of H_2O molecules, enhancing photocatalytic performance for CO_2 reduction in water vapor. Meanwhile, the stronger hydrophobicity of the film surface could ensure that the adsorbed sites of CO_2 on the surface were unoccupied by abundant H_2O molecules. The S-scheme charge transfer mode of $CuBi_2O_4/Bi_2O_3$ was further proposed for photocatalytic CO_2 reduction. This work may provide a promising S-scheme $CuBi_2O_4/Bi_2O_3$ film photocatalyst for photocatalytic CO_2 reduction, and meaningful information for hopefully stimulating more insightful investigations of systematical design and controlled assembly of visible-light-driven photocatalysts.

CRediT authorship contribution statement

Weina Shi: Conceptualization, Investigation, Resources, Writing – review & editing, Project administration. **Ji-Chao Wang:** Conceptualization, Methodology, Resources, Data Curation, Writing – original draft, Supervision, Funding acquisition. **Xiaowei Guo:** Methodology, Software, Formal analysis. **Hong-Ling Tian:** Validation, Formal analysis. **Wanqing Zhang:** Software, Data Curation, Investigation. **Huiling Gao:** Resources, Software. **Huijuan Han:** Validation, Visualization, Funding acquisition. **Renlong Li:** Writing – review & editing, Funding acquisition. **Yuxia Hou:** Formal analysis, Investigation, Funding acquisition.

Declaration of Competing Interest

The authors declare that they have no known competing financial interests or personal relationships that could have appeared to influence the work reported in this paper.

Acknowledgements

This work was supported by the financial supports of National Natural Science Foundation of China (Nos. 51802082 and 51903073), Natural Science Foundation of Henan Province (No. 212300410221), Program for Science & Technology Innovation Talents in Universities of Henan Province (No. 21HATIT016), Key Scientific Research Project of Colleges and Universities in Henan Province (No. 21A430030 and 20A150017), Key Scientific and Technological Project of Henan Province (No. 212102210473 and 202102310595) and "Climbing" Project of Henan Institute of Science and Technology (No. 2018CG04).

Appendix A. Supporting information

Supplementary data associated with this article can be found in the online version at doi:10.1016/j.jallcom.2021.161919.

References

[1] G. Chen, G.I.N. Waterhouse, R. Shi, J. Zhao, Z. Li, L.Z. Wu, C.H. Tung, T. Zhang, From solar energy to fuels: recent advances in light-driven C1 chemistry, Angew. Chem. Int. Ed. 58 (2019) 17528–175518, https://doi.org/10.1002/anie.201814313

[2] C. Wang, Y. Zhao, H. Xu, Y. Li, Y. Wei, J. Liu, Z. Zhao, Extensive solar light harvesting by integrating UPCL C-dots with Sn2Ta2O7/SnO2: highly efficient photocatalytic degradation toward amoxicillin, Environ. Pollut. 263 (2020) 114550, https://doi.org/10.1016/j.apcatb.2019.118314

[3] D. Xu, B. Cheng, W. Wang, C. Jiang, J. Yu, Ag_2CrO_4/g-C_3N_4/graphene oxide ternary nanocomposite Z-scheme photocatalyst with enhanced CO_2 reduction activity, Appl. Catal. B Environ. 231 (2020) 368–380, https://doi.org/10.1016/j.apcatb.2018.03.036

[4] W.A. Thompson, E.S. Fernandez, M.M. Maroto-Valer, Review and analysis of CO_2 photoreduction kinetics, ACS Sustain. Chem. Eng. 8 (2020) 4677–4692, https://doi.org/10.1021/acssuschemeng.9b06170

[5] Z. Wang, Z. Lin, J. Deng, S. Shen, F. Meng, J. Zhang, Q. Zhang, W. Zhong, L. Gu, Elevating the d-band center of six-coordinated octahedrons in Co_9S_8 through Fe-incorporated topochemical deintercalation, Adv. Energy Mater. 11 (2021) 2003023, https://doi.org/10.1002/aenm.202003023

[6] H. Guo, M. Chen, Q. Zhong, Y. Wang, W. Ma, J. Ding, Synthesis of Z-scheme α-Fe_2O_3/g-C_3N_4 composite with enhanced visible light photocatalytic reduction of CO_2 to CH_3OH, J. CO2 Util. 33 (2019) 233–241, https://doi.org/10.1016/j.jcou.2019.05.016

[7] Z. Lin, S. Shen, Z. Wang, W. Zhong, Laser ablation in air and its application in catalytic water splitting and Li-ion battery, iScience 24 (2021) 102469, https://doi.org/10.1016/j.isci.2021.102469

[8] A. Li, Q. Cao, G. Zhou, B.V.K.J. Schmidt, W. Zhu, X. Yuan, H. Huo, J. Gong, M. Antonietti, Three-phase photocatalysis for the enhanced selectivity and activity of CO_2 reduction on a hydrophobic surface, Angew. Chem. Int. Ed. 58 (2019) 14549–14555, https://doi.org/10.1002/anie.201908058

[9] Y. Xia, K. Xiao, B. Cheng, J. Yu, L. Jiang, M. Antonietti, S. Cao, Improving artificial photosynthesis over carbon nitride by gas–liquid–solid interface management for full light-induced CO_2 reduction to C1 and C2 fuels and O_2, ChemSusChem 13 (2020) 1730–1734, https://doi.org/10.1002/cssc.201903515

[10] W. Bi, Y. Hu, N. Jiang, L. Zhang, H. Jiang, X. Zhao, C. Wang, C. Li, Ultra-fast construction of plaque-like Li_2TiO_3/TiO_2 heterostructure for efficient gas-solid phase CO_2 photoreduction, Appl. Catal. B: Environ. 269 (2020) 118810, https://doi.org/10.1016/j.apcatb.2020.118810

[11] Y. Liu, D. Shen, Q. Zhang, Y. Lin, F. Peng, Enhanced photocatalytic CO_2 reduction in H_2O vapor by atomically thin Bi_2WO_6 nanosheets with hydrophobic and nonpolar surface, Appl. Catal. B: Environ. 283 (2021) 119630, https://doi.org/10.1016/j.apcatb.2020.119630

[12] J. Sun, J. Sun, X. Wang, Anatase TiO_2 with co-exposed (001) and (101) surfaces-based photocatalytic materials for energy conversion and environmental purification, Chem. Asian J. 15 (2020) 4168–4183, https://doi.org/10.1002/asia.202001085

[13] S. Shen, Z. Lin, K. Song, Z. Wang, L. Huang, L. Yan, F. Meng, Q. Zhang, L. Gu, W. Zhong, Reversed active sites boost the intrinsic activity of graphene-like cobalt selenide for hydrogen evolution, Angew. Chem. Int. Ed. 60 (2021) 12360–12365, https://doi.org/10.1002/anie.202102961

[14] R. Shi, Y. Chen, Controlled formation of defective shell on TiO_2 (001) facets for enhanced photocatalytic CO_2 reduction, ChemCatChem 11 (2019) 2270–2276, https://doi.org/10.1002/cctc.201900061

[15] N.N. Vu, S. Kaliaguine, T.O. Do, Critical aspects and recent advances in structural engineering of photocatalysts for sunlight-driven photocatalytic reduction of CO_2 into fuels, Adv. Funct. Mater. 29 (2019) 1901825, https://doi.org/10.1002/adfm.201901825

[16] Y. Ma, Z. Wang, X. Xu, J. Wang, Review on porous nanomaterials for adsorption and photocatalytic conversion of CO_2, Chin. J. Catal. 38 (2017) 1956–1969, https://doi.org/10.1016/S1872-2067(17)62955-3

[17] J. You, Y. Guo, R. Guo, X. Liu, A review of visible light-active photocatalysts for water disinfection: features and prospects, Chem. Eng. J. 373 (2019) 624–641, https://doi.org/10.1016/j.cej.2019.05.071

[18] Z. Wang, Z. Lin, S. Shen, W. Zhong, S. Cao, Advances in designing heterojunction photocatalytic materials, Chin. J. Catal. 42 (2021) 710–730, https://doi.org/10.1016/S1872-2067(20)63698-1

[19] A. Xu, W. Tu, S. Shen, Z. Lin, N. Gao, W. Zhong, $BiVO_4$@MoS_2 core-shell heterojunction with improved photocatalytic activity for discoloration of Rhodamine B, Appl. Surf. Sci. 528 (2020) 146949, https://doi.org/10.1016/j.apsusc.2020.146949

[20] Q. Xu, L. Zhang, B. Cheng, J. Fan, J. Yu, S-scheme heterojunction photocatalyst, Chem 6 (2020) 1–17, https://doi.org/10.1016/j.chempr.2020.06.010

[21] F. Xu, K. Meng, B. Cheng, S. Wang, J. Xu, J. Yu, Unique S-scheme heterojunctions in self assembled $TiO_2/CsPbBr_3$ hybrids for CO_2 photoreduction, Nat. Commun. 11 (2020) 4613, https://doi.org/10.1038/s41467-020-18350-7

[22] X. Jia, Q. Han, H. Liu, S. Li, H. Bi, F. Wang, A dual strategy to construct flowerlike S-scheme BiOBr/BiOAc1-Br heterojunction with enhanced visible-light photocatalytic activity, Chem. Eng. J. 399 (2020) 125701, https://doi.org/10.1016/j.cej.2020.125701

[23] C. Cheng, B. He, J. Fan, B. Cheng, S. Cao, J. Yu, An inorganic/organic S-scheme heterojunction H_2-production photocatalyst and its charge transfer mechanism, Adv. Mater. 33 (2021) 2100317, https://doi.org/10.1002/adma.202100317

[24] L. Luo, X. Shen, L. Song, Y. Zhang, B. Zhu, J. Liu, Q. Chen, Z. Chen, L. Zhang, MoS_2/Bi_2S_3 heterojunctions-decorated carbon-fiber cloth as flexible and filter-membrane-shaped photocatalyst for the efficient degradation of flowing wastewater, J. Alloy. Compd. 779 (2019) 599–608, https://doi.org/10.1016/j.jallcom.2018.11.154

[25] K. Wang, Z. Chen, M. Huang, Z. Yang, C. Zeng, L. Wang, M. Qiu, Y. Zhang, W. Zhang, A galvanic replacement reaction to synthesis of metal/ZnO heterostructured film on zinc substrate for enhanced photocatalytic performance, RSC Adv. 6 (2016) 103594–103600, https://doi.org/10.1039/C6RA23587E

[26] M. Gao, L. Zhu, W.L. Ong, J. Wang, G.W. Ho, Structural design of TiO_2-based photocatalyst for H_2 production and degradation applications, Catal. Sci. Technol. 5 (2015) 4703–4726, https://doi.org/10.1039/C5CY00879D
[27] D. Friedmann, A.F. Lee, K. Wilson, R. Jalili, R.A. Caruso, Printing approaches to inorganic semiconductor photocatalyst fabrication, J. Mater. Chem. A 7 (2019) 10858–10878, https://doi.org/10.1039/C9TA00888H
[28] U. Joost, K. Juganson, M. Visnapuu, M. Mortimer, A. Kahru, E. Nõmmiste, U. Joost, V. Kisand, A. Ivask, Photocatalytic antibacterial activity of nano-TiO_2 (anatase)-based thin films: Effects on Escherichia coli cells and fatty acids, J. Photochem. Photobiol. B 142 (2015) 178–185, https://doi.org/10.1016/j.jphotobiol.2014.12.010
[29] L. Wang, G. Yang, D. Wang, C. Lu, W. Guan, Y. Li, J. Deng, J. Crittenden, Fabrication of the flower-flake-like $CuBi_2O_4/Bi_2WO_6$ heterostructure as efficient visible-light driven photocatalysts: performance, kinetics and mechanism insight, Appl. Surf. Sci. 495 (2019) 143521, https://doi.org/10.1016/j.apsusc.2019.07.263
[30] L. Wang, T. Huang, G. Yang, C. Lu, F. Dong, Y. Li, W. Guan, The precursor-guided hydrothermal synthesis of $CuBi_2O_4/WO_3$ heterostructure with enhanced photoactivity under simulated solar light irradiation and mechanism insight, J. Hazard. Mater. 381 (2020) 120956, https://doi.org/10.1016/j.jhazmat.2019.120956
[31] Q. Chen, H. Long, M. Chen, Y. Rao, X. Li, Y. Huang, In situ construction of biocompatible Z-scheme α-$Bi_2O_3/CuBi_2O_4$ heterojunction for NO removal under visible light, Appl. Catal. B: Environ. 272 (2020) 119008, https://doi.org/10.1016/j.apcatb.2020.119008
[32] J.H. Kim, A. Adishev, J. Kim, Y.S. Kim, S. Cho, J.S. Lee, All-bismuth-based oxide tandem cell for solar overall water splitting, ACS Appl. Energy Mater. 1 (2018) 6694–6699, https://doi.org/10.1021/acsaem.8b01025
[33] F. Guo, M. Li, H. Ren, X. Huang, W. Hou, C. Wang, W. Shi, C. Lu, Fabrication of p-n $CuBi_2O_4/MoS_2$ heterojunction with nanosheets-on-microrods structure for enhanced photocatalytic activity towards tetracycline degradation, Appl. Surf. Sci. 491 (2019) 88–94, https://doi.org/10.1016/j.apsusc.2019.06.158
[34] W.-D. Oh, S.-K. Lua, Z. Dong, T.-T. Lim, Rational design of hierarchically-structured $CuBi_2O_4$ composites by deliberate manipulation of the nucleation and growth kinetics of $CuBi_2O_4$ for environmental applications, Nanoscale 8 (2016) 2046–2054, https://doi.org/10.1039/C5NR06223C
[35] K. Hakobyan, T. Gegenhuber, C.S.P. McErlean, M. Müllner, Visible-light-driven MADIX polymerisation via a reusable, low-cost, and non-toxic bismuth oxide photocatalyst, Angew. Chem. Int. Ed. 58 (2019) 1828–1832, https://doi.org/10.1002/anie.201811721
[36] P. Riente, M.A. Pericàs, Visible light-driven atom transfer radical addition to olefins using Bi_2O_3 as photocatalyst, ChemSusChem 8 (2015) 1841–1844, https://doi.org/10.1002/cssc.201403466
[37] X. Zhang, X. Wang, J. Chai, S. Xue, R. Wang, L. Jiang, J. Wang, Z. Zhang, D.D. Dionysiou, Construction of novel symmetric double Z-scheme $BiFeO_3/CuBi_2O_4/BaTiO_3$ photocatalyst with enhanced solar-light-driven photocatalytic performance for degradation of norfloxacin, Appl. Catal. B: Environ. 272 (2020) 119017, https://doi.org/10.1016/j.apcatb.2020.119017
[38] X. Yuan, D. Shen, Q. Zhang, H. Zou, Z. Liu, F. Peng, Z-scheme $Bi_2WO_6/CuBi_2O_4$ heterojunction mediated by interfacial electric field for efficient visible-light photocatalytic degradation of tetracycline, Chem. Eng. J. 369 (2019) 292–301, https://doi.org/10.1016/j.cej.2019.03.082
[39] Y. Wang, C. Liu, Y. Zhang, W. Meng, B. Yu, S. Pu, D. Yuan, F. Qi, B. Xu, W. Chu, Sulfate radical-based photo-fenton reaction derived by $CuBi_2O_4$ and its composites with α-Bi_2O_3 under visible light irradiation: catalyst fabrication, performance and reaction mechanism, Appl. Catal. B Environ. 235 (2018) 264–273, https://doi.org/10.1016/j.apcatb.2018.04.058
[40] W. Shi, F. Guo, M. Li, Y. Shi, M. Wu, Y. Tang, Enhanced visible-light-driven photocatalytic H_2 evolution on the novel nitrogen-doped carbon dots/$CuBi_2O_4$ microrods composite, J. Alloy. Compd. 775 (2019) 511–517, https://doi.org/10.1016/j.jallcom.2018.10.095
[41] A.C. Nogueira, L.E. Gomes, J.A.P. Ferencz, J.O.E.F.S. Rodrigues, R.V. Gonçalves, H. Wender, Improved visible light photoactivity of $CuBi_2O_4$/CuO heterojunctions for photodegradation of methylene blue and metronidazole, J. Phys. Chem. C 123 (2019) 25680–25690, https://doi.org/10.1021/acs.jpcc.9b06907
[42] Y. Sang, X. Cao, G. Dai, L. Wang, Y. Peng, B. Geng, Facile one-pot synthesis of novel hierarchical Bi2O3/Bi2S3 nanoflower photocatalyst with intrinsic p-n junction for efficient photocatalytic removals of RhB and Cr(VI), J. Hazard. Mater. 381 (2020) 120942, https://doi.org/10.1016/j.jhazmat.2019.120942
[43] J. Divya, N.J. Shivaramu, W. Purcell, W.D. Roos, H.C. Swart, Multifunction applications of Bi2O3:Eu3+ nanophosphor for red light emission and photocatalytic activity, Appl. Surf. Sci. 497 (2019) 143748, https://doi.org/10.1016/j.apsusc.2019.143748
[44] K.R.S. Devi, S. Mathew, R. Rajan, J. Georgekutty, K. Kasinathan, D. Pinheiro, S. Sugunan, Biogenic synthesis of g-C_3N_4/Bi_2O_3 heterojunction with enhanced photocatalytic activity and statistical optimization of reaction parameters, Appl. Surf. Sci. 494 (2019) 465–476, https://doi.org/10.1016/j.apsusc.2019.07.125
[45] H. Najafian, F. Manteghi, F. Beshkar, M. Salavati-Niasari, Fabrication of nanocomposite photocatalyst $CuBi_2O_4/Bi_3ClO_4$ for removal of acid brown 14 as water pollutant under visible light irradiation, J. Hazard. Mater. 361 (2019) 210–220, https://doi.org/10.1016/j.jhazmat.2018.08.092
[46] J.C. Wang, H.C. Yao, Z.Y. Fan, L. Zhang, J.S. Wang, S.Q. Zang, Z.J. Li, Indirect Z-scheme BiOI/g-C_3N_4 photocatalysts with enhanced photoreduction CO_2 activity under visible light irradiation, ACS Appl. Mater. Interfaces 8 (2016) 3765–3775, https://doi.org/10.1021/acsami.5b09901
[47] Y. Zhang, B. Xia, J. Ran, K. Davey, S.Z. Qiao, Atomic-level reactive sites for semiconductor-based photocatalytic CO_2 reduction, Adv. Energy Mater. 10 (2020) 1903879, https://doi.org/10.1002/aenm.201903879
[48] F. Fu, H. Shen, W. Xue, Y. Zhen, R.A. Soomro, X. Yang, D. Wang, B. Xu, R. Chi, Alkali-assisted synthesis of direct Z-scheme based Bi_2O_3/Bi_2MoO_6 photocatalyst for highly efficient photocatalytic degradation of phenol and hydrogen evolution reaction, J. Catal. 375 (2019) 399–409, https://doi.org/10.1002/aenm.201903879